Nested sampling of isobaric phase space for the direct evaluation of the isothermal-isobaric partition function of atomic systems

Blake A. Wilson,[1] Lev D. Gelb,[2] and Steven O. Nielsen[1]
[1]*Department of Chemistry, University of Texas at Dallas, Richardson, Texas 75080, USA*
[2]*Department of Materials Science and Engineering, University of Texas at Dallas, Richardson, Texas 75080, USA*

(Received 4 March 2015; accepted 5 October 2015; published online 21 October 2015)

Nested Sampling (NS) is a powerful athermal statistical mechanical sampling technique that directly calculates the partition function, and hence gives access to all thermodynamic quantities in absolute terms, including absolute free energies and absolute entropies. NS has been used predominately to compute the canonical (NVT) partition function. Although NS has recently been used to obtain the isothermal-isobaric (NPT) partition function of the hard sphere model, a general approach to the computation of the NPT partition function has yet to be developed. Here, we describe an isobaric NS (IBNS) method which allows for the computation of the NPT partition function of any atomic system. We demonstrate IBNS on two finite Lennard-Jones systems and confirm the results through comparison to parallel tempering Monte Carlo. Temperature-entropy plots are constructed as well as a simple pressure-temperature phase diagram for each system. We further demonstrate IBNS by computing part of the pressure-temperature phase diagram of a Lennard-Jones system under periodic boundary conditions. © *2015 AIP Publishing LLC.* [http://dx.doi.org/10.1063/1.4933309]

I. INTRODUCTION

In the context of molecular simulation, the partition function and consequently the absolute thermodynamic properties used to be considered inaccessible.[1] Metropolis[2] style Monte Carlo simulations provided a means to compute thermodynamic averages without direct knowledge of the value of the partition function. Similarly, various free energy methods, such as free energy perturbation and thermodynamic integration, have been developed to determine free energy differences without direct access to the partition function.[3] However, interest began to grow in the ability to compute the partition function and the absolute thermodynamic properties in fields such as pure substance reference data[4] and protein folding.[5] Methods such as Wang-Landau, multicanonical, and histogram reweighting have been developed in order to allow for computation of the density of states[6] (DOS) and consequently the partition function. However, most of these methods still struggle in the vicinity of phase transitions.[3,7] A relatively new athermal method called Nested Sampling (NS) provides a simple yet powerful way to compute partition functions while effortlessly handling phase transitions. Originally developed in the context of Bayesian computation by Skilling,[8,9] NS was designed to efficiently compute the evidence (partition function) of high dimensional spaces where the bulk of the probability is located in exponentially small regions.

NS was introduced in atomic simulation by Pártay *et al.*[7] to compute the canonical (NVT) partition function. Subsequently, NS has been used for the study of protein energy landscapes,[10] and the free energy of liquids and solids.[11–13] In a previous work, Nielsen extended NS to use NVT ensemble trajectories, such as those from molecular dynamics simulation.[14] Most recently, Pártay *et al.*[15] used NS to compute the isothermal-isobaric (NPT) partition function, but their method is restricted to the special case of the hard sphere model. In this work, we will demonstrate how NS can be adapted to compute the NPT partition function of a general atomic system.

The NPT ensemble closely reflects most experimental conditions (notably condensed phase systems) and is a common choice for the study of phase transitions.[16,17] NS computation of the NPT partition function opens up the possibility to study constant pressure properties, accurately characterize effects of pressure on phase transitions, and directly compute the Gibbs free energy and other thermodynamic quantities.

We first briefly review computation of the NVT partition function using NS. The configurational (momentum independent) portion of the NVT partition function, where the integrals have been reduced to a single dimension for simplicity of notation, can be written as

$$Q = \int_0^L e^{-\beta E(x)} dx, \tag{1}$$

with $\beta = 1/(kT)$ where k is the Boltzmann constant and $E(x)$ is the potential energy of configurational point x. The excess (non-ideal) portion of the partition function, Q_{ex}, is drawn out by applying the general coordinate scaling transformation $s = x/V^{1/3}$ where $V = L^3$ is the volume giving

$$\begin{aligned} Q &= V^N \int_0^1 e^{-\beta E(sV^{1/3})} ds \\ &= V^N Q_{ex}. \end{aligned} \tag{2}$$

In order to compute the excess partition function, a normalized uniform probability density of the scaled coordinate s, $p(s) = 1$, can be introduced giving

$$Q_{ex} = \int_0^1 p(s) e^{-\beta E(sV^{1/3})} ds. \tag{3}$$

Then, sampling from $p(s)$ could be performed and the excess partition function rewritten as

$$Q_{ex} = \lim_{n\to\infty} \frac{1}{n} \sum_{j=1}^{n} e^{-\beta E_j}, \tag{4}$$

a simple average over n potential energy values E_j evaluated at scaled configurational points randomly drawn from $p(s)$. However, Eq. (4) as written is impossible to accurately evaluate in finite time. This is due to the fact that the bulk of the thermal probability mass is located in an exponentially small region of low potential energy space. The NS algorithm, which is iterative in nature, provides a solution. Sample points in phase space are drawn at random from $p(s)$ and cataloged by their potential energy. After each iteration, a fixed high potential energy fraction, $1 - f$, of the remaining phase space volume is removed. The subsequent iteration continues to draw random samples from $p(s)$ but is restricted to the remaining low potential energy fraction of the phase space volume. Each successive iteration samples a low-energy subset of the previously sampled region of phase space; hence, successive samplings are nested within one another from one iteration to the next. This is demonstrated in the left panel of Figure 1 where each successive probability distribution of the potential energy overlaps (is nested within) the previous one. This iterative procedure naturally drives the sampling into the exponentially small low potential energy regions of phase space. The iterations continue until the algorithm converges to a minimum in the potential energy landscape. The NS simulation algorithm is as follows:

1. Sample configurations from $p(s)$, that is, uniformly in phase space, and construct a distribution of the corresponding potential energies;
2. determine the potential energy, E_i, at a fixed fraction, f, of the previously constructed potential energy distribution;
3. sample configurations from $p(s)$ under the condition $E < E_i$ and construct a new potential energy distribution; and
4. repeat steps 2 and 3 until some convergence/stopping criterion is met.

After the simulation is complete, the potential energy values E_i are used to approximate the excess partition function at any value of β by taking

$$Q_{ex} \approx \frac{1}{W_f} \sum_i \left(f^{i-1} - f^i\right) e^{-\beta(E_{i-1}+E_i)/2}, \tag{5}$$

where

$$W_f = \sum_i \left(f^{i-1} - f^i\right) \tag{6}$$

and $\left(f^{i-1} - f^i\right)$ is the fraction of phase space volume between nested potential energies E_{i-1} and E_i. $(E_{i-1} + E_i)/2$ is the arithmetic average of the two nested potential energies, which is used to approximate the average potential energy of configurations within that fraction of the phase space volume. NS thus allows for the direct computation of the partition function and all thermodynamic quantities at essentially any temperature from a single simulation. The use of a fixed phase space volume cutting fraction f also causes NS to naturally concentrate its efforts in the vicinity of large phase space volume changes and so is an ideal method for the study of first-order phase transitions.[7,14,15] In Secs. II–V, we modify the above algorithm to allow for computation of the NPT partition function, demonstrate the new isobaric Nested Sampling (IBNS) method on some simple finite atomic systems and confirm the results by comparing to parallel tempering (PT) Monte Carlo.[18] In addition, we further demonstrate IBNS under periodic boundary conditions on an atomic system of fixed box shape, in which we compute a small portion of the pressure-temperature phase diagram. We also outline the implementation of variable cell shape simulations for use with solids and liquid crystals.

II. ISOBARIC NESTED SAMPLING

The excess NPT partition function is given by

$$\begin{aligned}\Delta_{ex} &= \int_0^\infty dV e^{-\beta PV} Q(V) \\ &= \int_0^\infty dV e^{-\beta PV} V^N \int_0^1 e^{-\beta E(sV^{1/3})} ds.\end{aligned} \tag{7}$$

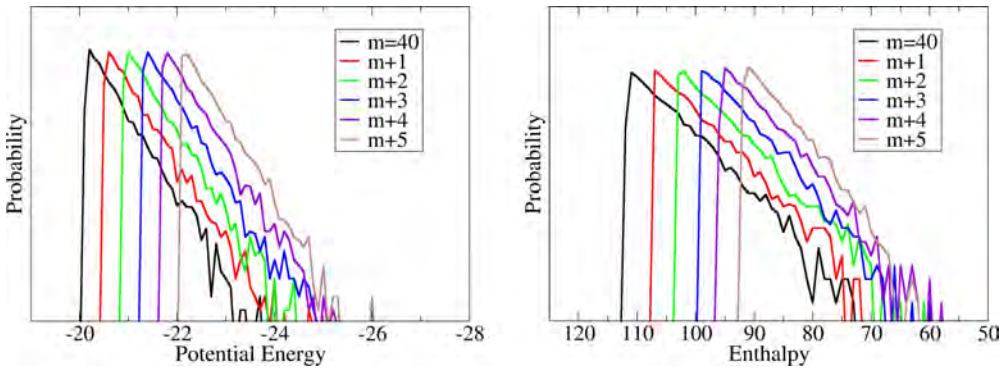

FIG. 1. Left: Potential energy probability distribution of nested sampling iteration m and five successive iterations with $f = 1/2$. The probability is plotted on a logarithmic scale. Right: Enthalpy probability distribution of nested sampling iteration m and five successive iterations with $f = 1/2$. The probability is plotted on a logarithmic scale. The values of potential energy and enthalpy are given in dimensionless units and are from isolated Lennard-Jones systems with 17 atoms under constant volume $V = 250$ (left) and constant pressure $P = 1.0$ (right).

The excess partition function can be written in terms of a normalized athermal probability density, $p(V,s)$,

$$\Delta_{ex} = K \int_0^\infty dV \int_0^1 p(V,s) e^{-\beta H} ds, \tag{8}$$

where $H = PV + E(sV^{1/3})$ is the enthalpy and

$$p(V,s) = \frac{V^N}{K} \tag{9}$$

with normalization constant K. Since the volume has no natural upper bound, it is necessary in practice to introduce an upper volume cutoff V_{max}. The excess partition function becomes

$$\Delta_{ex} = K \int_0^{V_{max}} dV \int_0^1 p(V,s) e^{-\beta H} ds, \tag{10}$$

with $K = V_{max}^{N+1}/(N+1)$. Samples could be drawn from $p(V,s)$ and the excess partition function reduced to

$$\Delta_{ex} = \lim_{n\to\infty} \frac{K}{n} \sum_{j=1}^{n} e^{-\beta H_j}, \tag{11}$$

a simple average over n enthalpy values H_j evaluated at isobaric phase space points drawn at random from $p(V,s)$. However, the bulk of the thermal probability mass exists in an exponentially small low-enthalpy region of the isobaric phase space. The NS algorithm again provides a solution. The sample points are cataloged by their enthalpy and athermal NS is performed on the isobaric phase space. This IBNS procedure iteratively eliminates high enthalpy regions of isobaric phase space, each corresponding to a fixed fraction $1-f$ of the remaining isobaric phase space volume. Each successive iteration thus samples a nested low-enthalpy subset of the previously sampled region of isobaric phase space. This is demonstrated in the right panel of Figure 1 where it can be seen that each successive probability distribution of the enthalpy overlaps the previous one. In order to draw samples from $p(V,s)$ using a Markov chain, new volumes, $V_1 \to V_2$, are accepted by the criteria

$$A(V_1 \to V_2) = min[1, (V_2/V_1)^N]. \tag{12}$$

Previous work[11–14] has established that a nested cutting fraction $f = 1/2$ often provides sufficient coverage of phase space to calculate the excess partition function. Although the method is not limited to this choice, we have used $f = 1/2$ and thus give the IBNS algorithm as follows:

1. Select a constant pressure value, P;
2. sample values of enthalpy according to $p(V,s)$ while enforcing $V \le V_{max}$;
3. determine the median enthalpy, H_m, of the enthalpy values sampled in the previous step;
4. sample values of enthalpy according to $p(V,s)$ under the conditions $H < H_m$ and $V \le V_{max}$; and
5. repeat steps 3 and 4 until some convergence/stopping criterion is met.

After the simulation is complete, the median enthalpy values (H_m) are used to approximate the excess partition function by taking

$$\Delta_{ex} \approx \frac{K}{W_f} \sum_m 2^{-m} e^{-\frac{\beta}{2}(H_{m-1}+H_m)}, \tag{13}$$

where in this case,

$$W_f = \sum_m 2^{-m} \tag{14}$$

and $2^{-m} = \left((1/2)^{m-1} - (1/2)^m\right)$ is the fraction of isobaric phase space volume between median enthalpies H_{m-1} and H_m and where $\frac{1}{2}(H_{m-1}+H_m)$ is the arithmetic average used to approximate the average enthalpy of isobaric configurations within that fraction of isobaric phase space.

Once the excess partition function has been defined, the full partition function is obtained within the semi-classical approximation by taking $\Delta_{NPT} \approx I_N Z_p \Delta_{ex}$ which includes the momentum contribution, Z_p, and the isothermal-isobaric pre-factor, I_N, which together are

$$I_N Z_p = \left[V_o N! \left(\frac{\beta h^2}{2\pi m} \right)^{3N/2} \right]^{-1}, \tag{15}$$

where h is Planck's constant, m is the particle mass, and V_o is the volume scaling factor. One common choice of volume scaling factor[17] is $V_o = 1/(\beta P)$. Subsequently, the absolute enthalpy would be given by $H = -\frac{\partial}{\partial\beta} \ln(I_N Z_p) + H_{ex}$ ($\approx \frac{5}{2}NkT + H_{ex}$, where the first term is the ideal gas contribution) and the absolute heat capacity by $C_P = -\frac{\partial}{\partial T}\frac{\partial}{\partial\beta} \ln(I_N Z_p) + C_{ex}$ ($\approx \frac{5}{2}Nk + C_{ex}$ where the first term is the ideal gas contribution). Similarly, the absolute free energy is written as $G = -kT \ln(I_N Z_p) + G_{ex}$ and the absolute entropy as $S = k \ln(I_N Z_p) - \frac{1}{T}\frac{\partial}{\partial\beta} \ln(I_N Z_p) + S_{ex}$. Namely, the thermodynamic quantities are separable into an excess contribution computed directly from IBNS and the contribution that comes from the definition of $I_N Z_p$ in the full partition function. Explicit expressions for the excess enthalpy, heat capacity, free energy, and entropy are as follows. The excess enthalpy H_{ex} is given by

$$\begin{aligned} H_{ex} &= -\frac{\partial}{\partial\beta} \ln(\Delta_{ex}) \\ &= \frac{K}{2\Delta_{ex}} \sum_m 2^{-m} (H_{m-1}+H_m) e^{-\frac{\beta}{2}(H_{m-1}+H_m)} \end{aligned} \tag{16}$$

and the excess heat capacity C_{ex} is given by

$$\begin{aligned} C_{ex} &= \frac{\partial H_{ex}}{\partial T} \\ &= \frac{K^2 \sum_m 2^{-m}(H_{m-1}+H_m) e^{-\frac{\beta}{2}(H_{m-1}+H_m)}}{2\Delta_{ex}^2} \\ &\quad \times \sum_m 2^{-m} \frac{(H_{m-1}+H_m)}{2kT^2} e^{-\frac{\beta}{2}(H_{m-1}+H_m)} \\ &\quad + \frac{K}{4kT^2\Delta_{ex}} \sum_m 2^{-m} (H_{m-1}+H_m)^2 e^{-\frac{\beta}{2}(H_{m-1}+H_m)}. \end{aligned} \tag{17}$$

Similarly, the excess free energy, G_{ex}, is given by

$$G_{ex} = -kT \ln(\Delta_{ex}) \tag{18}$$

and the excess entropy, S_{ex}, is given by

$$S_{ex} = k \ln(\Delta_{ex}) - \frac{1}{T}\frac{\partial}{\partial \beta} \ln(\Delta_{ex}). \quad (19)$$

Additionally, the expectation value of any momentum independent observable, O, can be determined through

$$\langle O \rangle = \frac{K}{\Delta_{ex}} \sum_m 2^{-m} O_m e^{-\frac{\beta}{2}(H_{m-1}+H_m)}, \quad (20)$$

where $O_m = \frac{1}{2}(\bar{O}_m + \bar{O}_{m-1})$, where $\bar{O}_m$ and $\bar{O}_{m-1}$ are the average values of O accumulated over IBNS iterations m and $m-1$.

III. FINITE LENNARD-JONES (LJ) SYSTEMS UNDER CONSTANT PRESSURE

LJ systems are a common choice for the testing of new simulation methods. We have chosen to simulate two small finite LJ systems with 17 and 55 particles denoted LJ_{17} and LJ_{55}, respectively. In addition to proving the efficacy of IBNS, we highlight some interesting pressure effects on these finite LJ systems and construct simple phase diagrams for each one. Parallel tempering Monte Carlo simulations were run to confirm the accuracy of IBNS.

A. Simulation details — Isobaric nested sampling

The standard pairwise additive 12-6 LJ interaction potential was used for particle interactions. All simulations were run in reduced LJ units, taking σ as the unit of distance and ϵ as the unit of energy, and data are reported in these reduced LJ units. There is no cutoff on the LJ potential and the boundary is a hard sphere with radius $R = \left(\frac{3V}{4\pi}\right)^{1/3}$ which is centered on the center of mass of the particle configuration. Simulations were run at pressures of 0.001, 0.01, 0.1, and 1.0. A simple Monte Carlo sampler with two Markov chains launched from the same starting configuration and run in parallel was used during each IBNS iteration. Each Markov chain consisted of single-atom translations and isotropic volume deformations. Volume deformations were performed every $2N$ trial moves, where N refers to the number of LJ particles, while all other trial moves were single atom translations. Each Markov chain executed $40\,000N$ initial trial moves during which no data were collected followed by 4.0×10^6 trial moves during which data were collected every $10N$ trial moves. The coordinates for this style of simulation boundary tend to drift over long trajectories, so after every $5N$ trial moves, the center of mass was moved back to the origin. Instead of defining a strict upper volume cutoff, an upper enthalpy cutoff, H_{max}, of 800.0 was used for both LJ_{17} and LJ_{55} at all pressures. H_{max} was assumed to be sufficiently high that the simulations started in regions of isobaric phase space dominated by ideal gas behavior and the upper volume cutoff approximated as $V_{max} \approx H_{max}/P$. The initial structure in the first iteration of the IBNS loop for both Markov chains was taken as the global energy minimum cluster (http://doye.chem.ox.ac.uk/jon/structures/LJ/tables.150.html) with an initial volume set to V_{max}. The starting coordinates could have equally well been generated at random within the initial volume as long as the initial enthalpy was $\leq H_{max}$. During each IBNS iteration, the lowest enthalpy configuration (volume and coordinates) visited was stored and used as the initial condition for the next iteration. During each iteration of the IBNS loop a distribution of enthalpy values was constructed and the nested enthalpy, H_m, was taken as the median of this distribution. Trial move acceptance ratios were separately monitored for both particle translations and volume deformations. When the trial move acceptance ratio for one of these move types dropped below 30% in an iteration, the trial move size was decreased by a factor of 0.2–0.75, dependent on how far below 30% the acceptance was before the next iteration. This was done in order to maintain acceptance ratios of approximately 30%-50% for most iterations. The simulation was considered converged when $|H_m - H_{m-1}| < 1.0 \times 10^{-4}$ and this required between 400-700 nested iterations for LJ_{17} and 1500-2100 for LJ_{55}. For both LJ systems, ten separate IBNS simulations were run for each pressure. The IBNS simulation output was used to generate data at 1×10^3 temperatures from $T = 1.0 \times 10^{-3}$ to $T = 2$ with constant temperature spacing $\Delta T = 1.99 \times 10^{-3}$. The reported IBNS data were computed as the average of data from the ten separate simulations and the error bars were subsequently computed as two times the standard error of those averages, corresponding to 95% confidence intervals. Pseudo-random numbers were generated using the double precision single instruction multiple data (SIMD)-oriented Fast Mersenne Twister (http://www.math.sci.hiroshima-u.ac.jp/~m-mat/MT/SFMT/index.html) which uses the algorithm described by Saito and Matsumoto.[19]

B. Simulation details — Parallel tempering

PT Monte Carlo calculations were performed using our own code as follows. The same boundary treatment was applied as described for the IBNS simulations. Particle displacement moves and volume-change moves were attempted with relative frequencies of 50 displacements per volume-change move. Simulations were run for at least 2×10^8 trial moves, with the first 10^7 moves discarded for equilibration. Data were collected every 10^4 (N = 17) or 2×10^4 (N = 55) trial moves. The temperatures shown were all simulated in a single run, with temperature-swap moves performed every 1000 (N = 17) or 2000 (N = 55) trial moves, though in a few cases, a second run was made to cover 1–3 additional temperatures near significant peaks. Uncertainties in the reported data were calculated by dividing the runs into $M = 20$ blocks and calculating standard deviations σ_b (of each quantity) of the block averages; the reported uncertainties are given by $d_{PT}(T) = 2\sigma_b/\sqrt{M}$ and correspond to 95% confidence estimates.

C. Results and discussion

1. Comparison to parallel tempering Monte Carlo

The excess heat capacity per particle and number density are verified with PT Monte Carlo. Figure 2 shows results for LJ_{55} at the four simulated pressures. The corresponding results for LJ_{17} are shown in Figure 3. There is very good agreement between IBNS and PT for both systems at all four

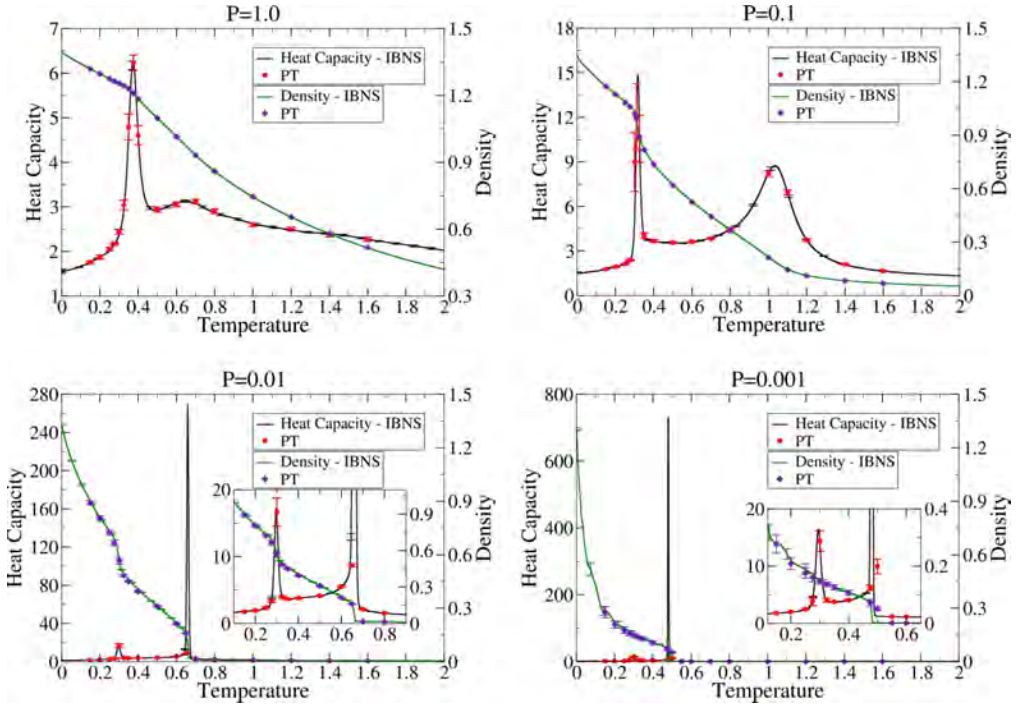

FIG. 2. Heat capacity (excess per particle) and density versus temperature for LJ_{55} at pressures 1.0, 0.1, 0.01, and 0.001 computed by isobaric Nested Sampling (IBNS) and Parallel Tempering (PT) Monte Carlo simulation. The isobaric NS plots are essentially continuous so the error bars are only shown for some of the points. Error bars of the density at pressures 1.0 and 0.1 are on the order of the plot line thickness, so are not included.

pressures. The agreement was further examined by computing the average absolute percent difference, $\%_D$, for the heat capacity at pressures 1.0 and 0.1, where

$$\%_D = \frac{100\%}{n_{PT}} \sum_{i=1}^{n_{PT}} \frac{|C_P^{NS}(T_i) - C_P^{PT}(T_i)|}{C_P^{PT}(T_i)} \tag{21}$$

in which n_{PT} is the total number of PT data points. This was compared to the average percent uncertainty in the PT data, $\%_d$, where

$$\%_d = \frac{100\%}{n_{PT}} \sum_{i=1}^{n_{PT}} \frac{d_{C_P}^{PT}(T_i)}{C_P^{PT}(T_i)} \tag{22}$$

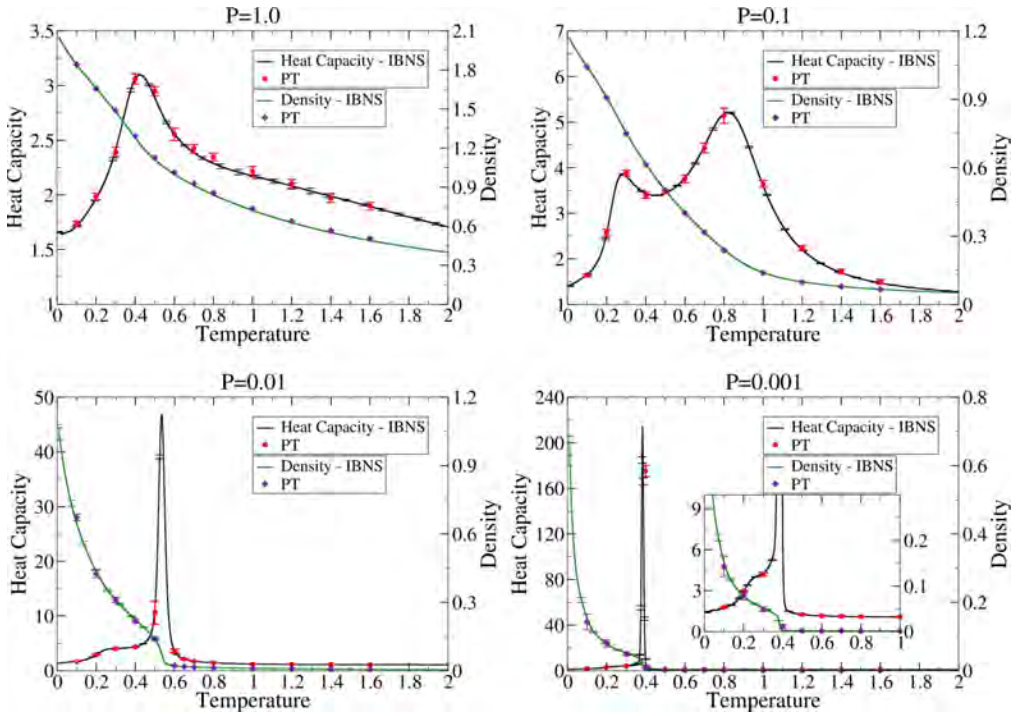

FIG. 3. Heat capacity (excess per particle) and density versus temperature for LJ_{17} at reduced pressures 1.0, 0.1, 0.01, and 0.001 computed by isobaric Nested Sampling (IBNS) and Parallel Tempering Monte Carlo (PT) simulation. The isobaric NS plots are essentially continuous so the error bars are only shown for some of the points. Error bars of the density at pressures 1.0 and 0.1 are on the order of the plot line thickness, so are not included.

TABLE I. Comparison of the average percent difference, $\%_D$, in the parallel tempering and corresponding isobaric nested sampling heat capacity data to the average percent uncertainty, $\%_d$, in the parallel tempering heat capacity data. Values are truncated after the first decimal.

LJ_N	P	$\%_D$	$\%_d$	$\%_D/\%_d$
55	1.0	1.1	2.3	0.4
55	0.1	3.2	4.7	0.6
17	1.0	1.0	1.7	0.5
17	0.1	1.1	2.3	0.4

in which $d_{C_P}^{PT}(T_i)$ is the uncertainty estimate in the PT heat capacity. The heat capacity is a good choice for this comparison because it is a second derivative of the logarithm of the partition function and is thus very sensitive to error or noise. The results of this comparison are given in Table I and demonstrate that the IBNS data points are well within the estimated uncertainty of the PT data.

2. Pressure effects on phase transitions

The pressure can greatly influence structure and phase changes. For example, in a study of LJ_{38}, Freeman *et al.*[20] demonstrated that increased pressure could completely eliminate the lowest temperature cluster reorganization (solid-solid) phase change. Doye and Calvo[21] also demonstrated the importance of the pressure on the solid structure of nanoclusters. Here the effects of the pressure on the heat capacity and the phase transitions as observed for LJ_{55} and LJ_{17} will be discussed.

First we consider LJ_{55} (Figure 2). At all pressures, there is a low temperature solid-liquid transition, characterized in previous studies.[22–24] The lower three pressures also exhibit a liquid-gas transition at higher temperature. This is verified by examining the density plots shown in Figure 2. By $P = 1.0$, the higher-temperature peak in C_p has nearly disappeared, and the density is quite high over the corresponding temperature range. This suggests a state reminiscent of the bulk supercritical fluid (that is, that $P = 1.0$ is above the "critical" pressure in this finite system), although no structural characterization was performed to quantify this. In addition, for $P = 1.0$ at $T \approx 0.65$, there is a small but broad peak in the heat capacity. This is an interesting result because no transition in this region was expected. It perhaps suggests that some form of liquid-liquid reordering occurs. However, without further structural analysis, we cannot accurately characterize this transition. It is also clear that the pressure affects the transition temperatures. The transition temperature tends to increase with pressure, consistent with previous studies[21,23] of LJ solids. At sufficiently low pressure (below the triple point), there should exist a single sublimation type transition at the merging of the two distinct peaks in the heat capacity. This trend is evidenced by the decrease in the temperature gap between the two transitions with decreased pressure. The peaks of the heat capacity tend to broaden as the pressure increases, most noticeably for the liquid-gas transition peak. This is best demonstrated by the change from $P = 0.01$ to $P = 0.1$. This peak broadening has been reported before for the solid-liquid transition.[23]

In LJ_{17} (Figure 3), similar behavior is seen. At $P = 0.001$ and $P = 0.01$, there is a sharp liquid-gas phase transition peak in the heat capacity while the solid-liquid transition appears as a shoulder on that peak. The solid-liquid transition peak in the heat capacity is only clearly visible starting at $P = 0.1$. At $P = 1.0$, the system is in a supercritical fluid state above the solid-liquid boundary. The broadening of the heat capacity peaks with increasing pressure is also clearly visible in LJ_{17}.

3. Temperature-entropy plots

Temperature-entropy (TS) plots consist of isobars of the temperature versus entropy. First-order phase transitions appear in the TS plot as horizontal lines where the entropy changes but the temperature does not. From sufficient data, one can construct phase diagrams.[25]

The excess entropy is computed using Eq. (19). The TS plots for LJ_{55} are displayed in the left panel of Figure 4. The TS plot clearly highlights the liquid-gas coexistence regions, but the solid-liquid transition is less obvious due to the very small difference in entropy between the liquid and solid across the transition. It is also clear that ΔS_{ex} of the phase transitions decreases with increasing pressure. The aforementioned trend of increased transition temperature with pressure is also visible in the TS plot and the absence of a sharp liquid-gas transition at $P = 1.0$ is noticeable. It is also interesting to note that the

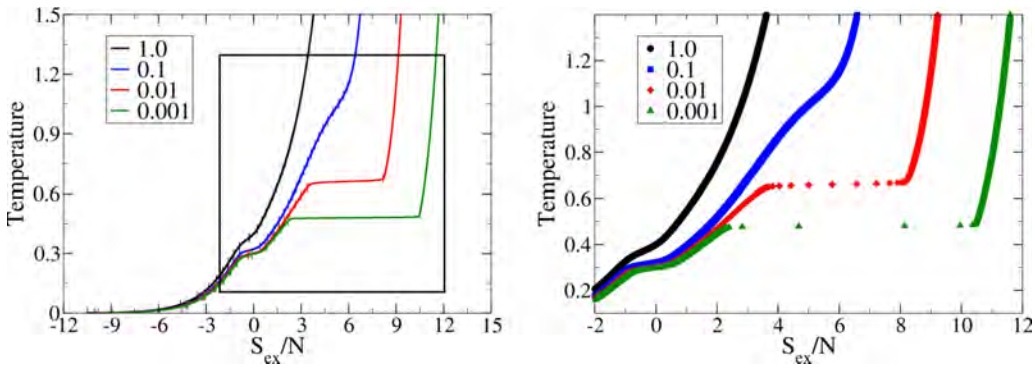

FIG. 4. Left: Temperature versus (excess) entropy per particle (TS) plots for LJ_{55} at various pressures as computed from nested sampling. Note that the error bars are in the entropy and are displayed at intervals of 20 data points. Right: Inset to highlight the liquid-gas transition region, with data displayed as points without error bars. Since the data was computed on an equally spaced temperature grid ($\Delta T = 1.99 \times 10^{-3}$) the slope across the transition is apparent from the density of data points within it.

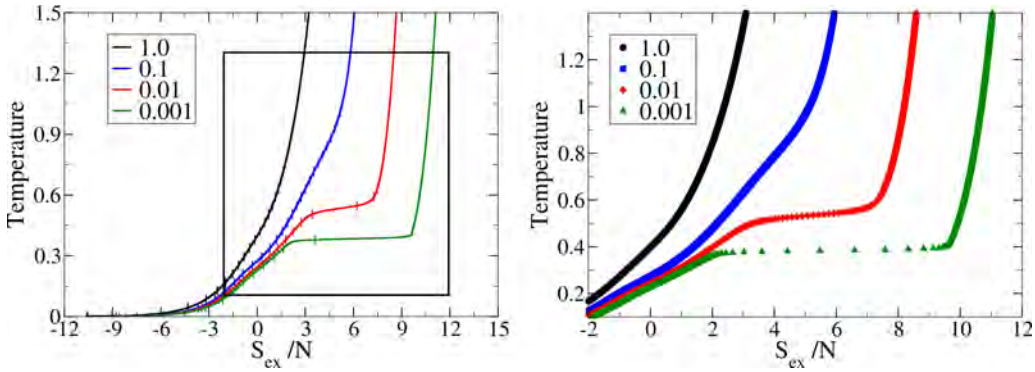

FIG. 5. Left: Temperature versus (excess) entropy per particle (TS) plots for LJ_{17} at various pressures as computed from nested sampling. Note that the error bars are in the entropy and are displayed at intervals of 20 data points. Right: Inset to highlight the liquid-gas transition region, with data displayed as points without error bars. Since the data were computed on an equally spaced temperature grid ($\Delta T = 1.99 \times 10^{-3}$), the slope across the transition is apparent by the density of data points within it.

slope across the transitions appears to increase with pressure. The effect is more dramatic for the liquid-gas transition and is highlighted in the right panel of Figure 4. This suggests that the phase changes become more continuous as the pressure is increased. The TS plots for LJ_{17} are shown in Figure 5. Again, results similar to LJ_{55} are seen for LJ_{17}, although there is one marked difference. The solid-liquid transition for LJ_{17} is essentially unnoticeable in the TS plot. Unlike LJ_{55} which forms a perfect icosohedral cluster,[22,23,26] LJ_{17} forms a cluster with an icosohedral LJ_{13} core and an anti-Mackay over-layer[26] where the over-layer atoms are more fluid-like with higher entropy. This likely leads to a smaller change in entropy across the solid-liquid boundary of LJ_{17} and a more continuous liquid-solid transition at all pressures.

4. Pressure-temperature phase diagrams

The constant pressure heat capacity results can be used to construct pressure-temperature phase diagrams.[23,24] This is done by estimating the transition temperatures from the peaks in the heat capacity data. Combining the transition temperatures for several pressures then allows coexistence lines to be constructed.

The phase diagram estimated in this way for LJ_{55} is shown in the left panel, and for LJ_{17} in right panel, of Figure 6. $P = 1.0$ was not included due to the absence of a liquid-gas transition. For clearly defined peaks, the transition temperature was estimated by finding the local maximum in the heat capacity across the transition. However, the solid-liquid peaks for LJ_{17} at $P = 0.01$ and $P = 0.001$ appear as shoulders on the liquid-gas transition peaks, and so were not clearly discernible using local maxima. Therefore, these values were estimated by taking the numerical derivative of the heat capacity across the shoulder and finding the point closest to zero. Clearly, inclusion of more pressures could allow a much more complete phase diagram to be constructed.

5. Additional computational considerations

LJ_{55} and LJ_{17} systems were chosen for this study due to the funnel-like nature of their potential energy landscapes,[27] which results in a low complexity enthalpy landscape. This in turn should allow the simple Monte Carlo sampler as implemented here to be sufficient. This assumption was confirmed by running ten independent simulations at each pressure, which produced consistent results. Namely, it was found that the Markov chains did not become trapped in higher enthalpy local minima and that all runs at each pressure converged to the same minimum. For more complex systems there is a greater chance of trapping in local enthalpy minima as the NS iterations progress. However, there are more sophisticated sampling schemes which can alleviate this issue. These include techniques such as employing multiple walkers,[7,28] more advanced move-sets such as cluster moves,[17]

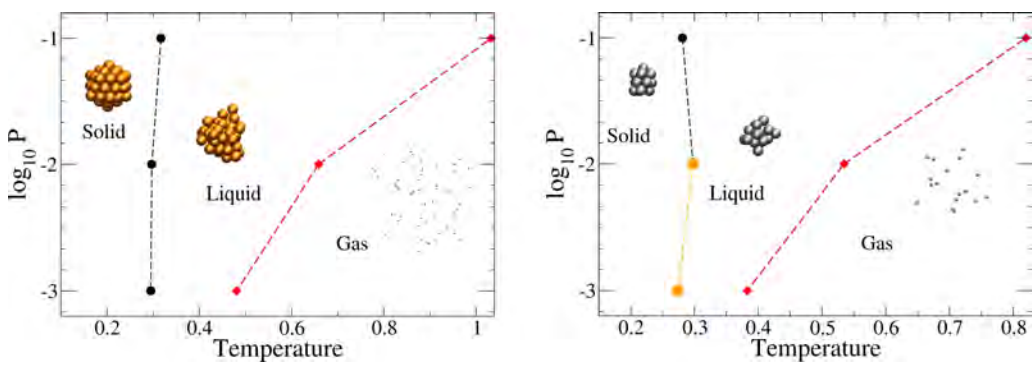

FIG. 6. Left: Pressure-temperature phase diagram for LJ_{55}. Right: Pressure-temperature phase diagram for LJ_{17}. Solid-liquid transitions for LJ_{17} at pressures of 0.001 and 0.01 exhibited shoulders rather than well-defined peaks; the shoulder locations were determined from the curvature inflection points and are marked in orange. The dashed lines were added to help guide the eye.

as well as enhanced NS algorithms including diffusive[11,29] and superposition enhanced[30] NS. It should also be possible to implement any biased move-set in which the bias can be easily removed.[14,31] Another potential sampler improvement to IBNS may be the use of NPT molecular dynamics trajectories in place of Markov chains in a manner analogous to that demonstrated by Nielsen.[14] Such an update may increase the speed and efficiency, as well as ease of application, of IBNS, especially for larger and more complex atomic/molecular systems.

In this work, the enthalpy distributions used to determine the median enthalpy values were constructed using a histogram with a bin width of 1.0×10^{-4}. The median enthalpy was determined by normalizing the histogram and integrating to one half of the total area. A practical concern when using histograms is the bin width, which should be small. The median enthalpy can also be rigorously constructed by collecting a list of enthalpy values, sorting the list, and taking the midpoint value of the sorted list. We checked that the histogram bin width used was sufficiently small to obtain the same median value as obtained from the list approach.

Additional simulations of LJ_{17} at P = 1.0 were run to probe the dependence on simulation parameter choices. Since there is no natural upper bound on the volume, it was necessary to employ an upper volume cutoff (V_{max}) in the IBNS simulation. Simulations of LJ_{17} at P = 1.0 were run with different values of V_{max} and the effects on two of the thermodynamic quantities are shown in Figure 7. V_{max} has the largest effect on the quantities that depend directly on the logarithm of the partition function such as the free energy and entropy, as demonstrated in the left panel of Figure 7. As demonstrated in the right panel of Figure 7, the quantities such as enthalpy and heat capacity, which depend on derivatives of the logarithm of the partition function, as well as other observables ($\langle O \rangle$), are much less sensitive to V_{max}.

The upper volume cutoff (V_{max}) should in general correspond to a system behavior approaching that of an ideal gas. That is, the enthalpy distribution under V_{max}, in thermally unbiased phase space, should be dominated by high volume configurations, rather than high potential energy configurations. The choice of an appropriate value for the upper volume cutoff will depend on the system size, strength and range of interactions, as well as the pressure. A conservative first choice would be to simply set the upper volume cutoff to an extremely large value. However, depending on the pressure and system size, the computational cost of increasing the upper volume cutoff can become quite large. The simulation efficiency can be increased by minimizing V_{max} to a value that is just large enough to still start the simulation in a region of isobaric phase space which is dominated by ideal gas like behavior. Comparison of the first median enthalpy H_1 to V_{max} leads to a simple way to check whether the upper volume cutoff is sufficiently large to do this. For upper volume cutoffs of 800 and 2000 it was found that the ratio $H_1/(PV_{max})$ ranges from approximately 0.95 to 0.98, while for the upper volume cutoff of 200, it is well above one. Therefore, if $H_1/(PV_{max}) > 1.0$, the upper volume cutoff is likely too small and should be increased to a value where $H_1/(PV_{max}) < 1.0$ in order to capture the ideal gas limiting behavior. To further demonstrate this concept, simulations were run in which an upper potential energy cutoff, E_{max}, for the system at volume V_{max} is used. This gives a corresponding upper enthalpy cutoff, $H_{max} = PV_{max} + E_{max}$, which can be applied in the first IBNS iteration such that accepted trial moves must follow both $V \leq V_{max}$ and $H \leq H_{max}$. Figure 8 displays the logarithm of the first median enthalpy for LJ_{17} at P = 1.0 plotted versus E_{max} at three values of V_{max}. Figure 8 shows that if V_{max} is taken to be sufficiently high then as long as $E_{max} \geq 0$, there is little effect on the first median enthalpy. This is consistent with the assumption that the simulation initially samples a region of isobaric phase space which is dominated by ideal gas like behavior. That is, even though high potential energy configurations can be accessed more readily at lower volumes, they contribute little to the overall enthalpy distribution for volumes at and near V_{max}. Therefore, for sufficiently large V_{max}, the upper enthalpy cutoff can safely be taken as $H_{max} = PV_{max}$. The converse is true for the system with $V_{max} = 200$. Since the upper volume cutoff is below the threshold of ideality, the higher potential energy states contribute significantly to the enthalpy distribution. This is seen in Figure 8 by the significant increase of H_1 with E_{max} for $V_{max} = 200$.

It should be noted that the upper volume cutoff, even one that satisfies the $H_1/(PV_{max}) < 1.0$ criteria, will always limit the very high temperature accuracy of the free energy, entropy, and some configuration dependent observables. This is also true for the free energy and entropy at very low pressures, where the high volume ideal gas like states contribute more significantly to the partition function. However, a simple

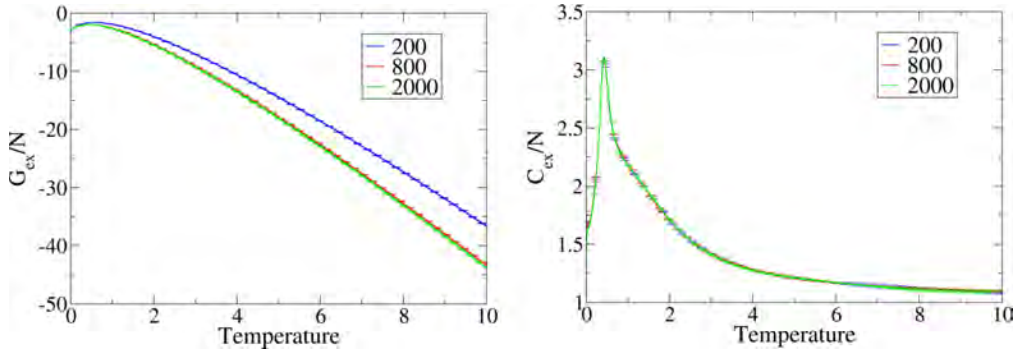

FIG. 7. Left: Comparison of the excess free energy per particle (G_{ex}/N) for maximum volume (V_{max}) values 200, 800, and 2000. Right: Comparison of the excess heat capacity per particle (C_{ex}/N) for maximum volume (V_{max}) values 200, 800, and 2000. Error bars are the standard deviation of data from three separate simulations.

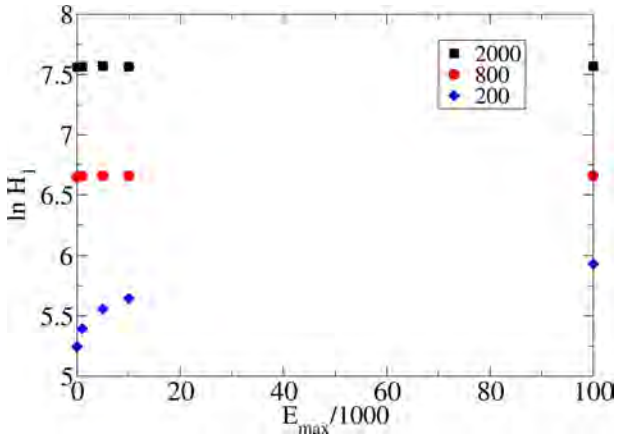

FIG. 8. Natural logarithm of the first nested enthalpy value ($H_{m=1}$) versus the maximum energy per thousand at maximum volume (V_{max}) values 200, 800, and 2000. Error bars were computed as the standard deviation of three separate simulations but are smaller than the size of the data point symbols.

correction can be added to the partition function, which will allow very high temperature and low pressure free energy and entropy values to be computed more accurately. This is done by taking $\Delta_{ex} + \int_{V_{max}}^{\infty} V^N e^{-\beta PV} dV$, which approximates the isobaric configurations with $V > V_{max}$ to be an ideal gas. If the temperature region of interest corresponds to properties very far from the ideal gas limit then the upper volume cutoff may be reduced even further (where $H_1/(PV_{max}) > 1.0$). This lowering of the upper volume cutoff will allow quantities such as average enthalpy and heat capacity, which depend on derivatives of the logarithm of the partition function, to be computed accurately at lower temperatures for reduced computational cost, but will limit the accuracy of the free energy, entropy, and some observables $\langle O \rangle$.

Finally, simulations of LJ_{17} at P = 1.0 were run with different Markov chain lengths in order to demonstrate how the chain length choice can affect the median enthalpy values. The left panel of Figure 9 demonstrates how the median enthalpy values can systematically shift from one iteration to the next if the Markov chain length is too small, while the right panel of Figure 9 shows that the error in the first median enthalpy can become large if the Markov chain length is too small. Longer Markov chains typically will produce better quality median enthalpy values (lower error) which introduces a trade-off between performance and accuracy.

The simulations in this work were not designed for performance comparison; PT was used simply to confirm correctness of the new IBNS method. However, a rough performance comparison is as follows: approximately 14 times more computational effort (characterized by the total number of pair-wise energy computations) was invested in IBNS with a corresponding six-fold reduction in the uncertainty of the heat capacity. Since the typical error reduction follows as the square root of the invested effort, this suggests that this version of IBNS sampled approximately 2.5 times more efficiently than PT on average. In a detailed comparison of NS and PT for computing the canonical heat capacity of similar LJ cluster systems Pártay *et al.*[7] reported significant performance gains of NS over PT, which increased with system size. In addition, the NS output can be used to directly compute much more thermodynamic data than PT (e.g., absolute free energy and entropy).

It is important to note that PT typically struggles in the vicinity of phase transitions; without prior knowledge of their location, it is generally difficult to set a temperature schedule that will accurately identify them and have effective exchange between replicas. Indeed, the IBNS results were used to add some additional PT temperature points in the vicinity of phase transitions for some of the simulated systems. For example, in this work, PT failed to locate the liquid-gas phase transition of LJ_{55} at $P = 0.001$ due to its sharpness. This problem for PT is exacerbated for larger system sizes and lower pressures as the phase transition becomes sharper and the heat capacity peak narrower. This is because the ideal temperature schedule for PT will place replicas with temperature spacing $\Delta T \propto T/C^{1/2}$, where C is the heat capacity.[32] This means many more replicas are required in the vicinity of the phase transition to insure the most effective sampling in PT. Methods such as that reported by Katzgraber *et al.*[33] do provide an iterative solution to optimize the PT temperature schedule. In contrast, NS requires no such optimization.

Another important aspect of any technique in today's high performance computing environment is parallelization. Although each subsequent energy (in this case enthalpy) subdivision follows serially from the previous one in NS, the sampling routine can be effectively parallelized in the manner demonstrated by Burkoff *et al.*,[10] or that proposed by Henderson and Goggans,[34] or in the manner used in this work. Like many simulation methods NS could also benefit

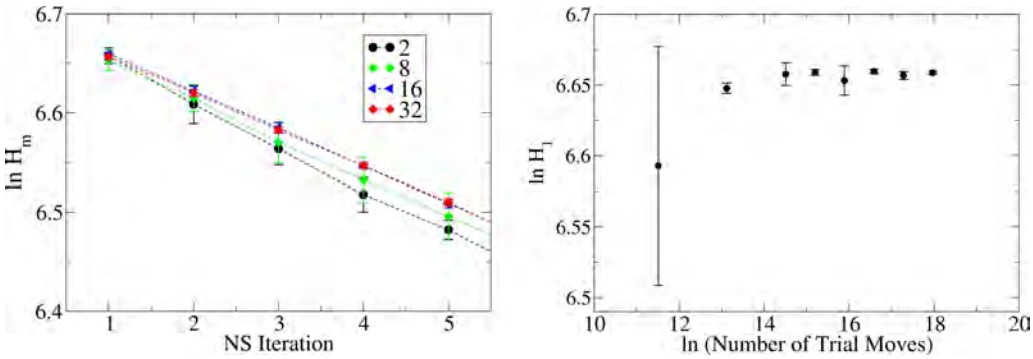

FIG. 9. Left: Comparison of the natural logarithm of the first five nested enthalpy values (H_m) using 2, 8, 16, and 32 ($\times 10^6$) total post-equilibration trial moves. Right: Logarithm of the first nested enthalpy value ($H_{m=1}$) plotted against the logarithm of the total number of post-equilibration trial moves used to build the distribution of enthalpies in the first IBNS iteration. Error bars are the standard deviation of values from three separate simulations.

from additional parallelization of sub-routines such as pair-wise energy computations in larger systems.

IV. LENNARD-JONES SYSTEM WITH PERIODIC BOUNDARIES

In Sec. III, we demonstrated the power of IBNS with simple finite (non-periodic) LJ systems. In this section, we demonstrate the use of IBNS on a periodic LJ system of fixed box shape by computing a portion of the pressure-temperature phase diagram. We also outline the extension to variable cell shape systems.

A. Simulation details — Isobaric nested sampling

A system size of $N = 128$ particles was simulated using the standard pairwise additive 12-6 LJ interaction potential. All simulations were run in reduced LJ units, taking σ as the unit of distance and ϵ as the unit of energy, and data are reported in these reduced LJ units. The interactions were truncated with a radial cutoff distance $r_c = 2.5$ and periodic interactions were computed using the minimum image convention. No long range corrections were considered. Simulations were run at four different pressures: 0.025, 0.050, 0.100, and 0.1500. The simulation cell was cubic with $V_{max} = 750.0$ (the maximum allowed volume corresponding to a minimum density of 0.1706) and an upper enthalpy cutoff $H_{max} = 200.0 + PV_{max}$. Additionally, the edge length of the cubic unit cell was restricted to be greater than or equal to $2r_c$, which corresponds to an effective upper density cap of 1.024. Limiting the density range in this way reduces the computation time. It should have negligible effects on intervening properties where the average density is between the upper and lower density caps. For example, McNeil-Watson and Wilding[38] reported solid phase densities of ~0.96 at the solid-liquid coexistence. Wilding[35] also reported a critical density of 0.3197(3) for this model. A simple Monte Carlo sampler with a single Markov chain was used to collect samples during each IBNS iteration. The Markov chain consisted of single-atom translations and isotropic volume deformations. Volume deformations were performed every $2N$ trial moves, where N refers to the number of LJ particles, while all other trial moves were single atom translations. The Markov chain executed $5000N$ initial trial moves during which no data were collected followed by 2.56×10^6 trial moves during which data were collected every $20N$ trial moves. The starting coordinates were generated at random within the initial volume V_{max}. During each IBNS iteration, the lowest enthalpy configuration (volume and coordinates) visited was stored and used as the initial condition for the next iteration. During each iteration of the IBNS loop a distribution of enthalpy values was constructed and the nested enthalpy, H_m, was taken as the median of this distribution. Trial move acceptance ratios were separately monitored for both particle translations and volume deformations. When the trial move acceptance ratio for one of these move types dropped below 30% in an iteration, the trial move size was decreased by a factor of 0.2–0.75, dependent on how far below 30% the acceptance was before the next iteration. This was done in order to maintain acceptance ratios of approximately 30%-50% for most iterations. Five separate IBNS simulations were run with different random number seeds at each pressure. Each simulation was considered converged when $|H_m - H_{m-1}| < 1.0 \times 10^{-2}$ and this required between 1900-2100 nested iterations. The reported IBNS data were computed as the average of data from the five separate simulations and the error bars were subsequently computed as two times the standard error of those averages, corresponding to 95% confidence intervals.

B. $N = 128$ Lennard-Jones pressure-temperature phase diagram

The heat capacity data were analyzed in a manner similar to that used in Section III C 4 to determine the transition temperatures for both the solid-liquid and liquid-gas phase transitions. The corresponding pressure-temperature phase diagram is shown in Figure 10. The critical temperature $T_c = 1.1876(3)$ and pressure $P_c = 0.1093(6)$ were previously reported by Wilding[35,36] for the same choice of potential cutoff. Potoff and Panagiotopoulos[37] later reported comparable results, with $T_c = 1.186(2)$ and $P_c = 0.109(2)$. Although greater than P_c, the highest simulated pressure $P = 0.150$ displayed a small broad peak in the heat capacity at $T \approx 1.25$. This is demonstrated in Figure 11, which shows the entropy and heat capacity results at each pressure in the region of the liquid-gas coexistence. There is some rounding of the transition entropies due to the small system size; regardless, it is clear that the entropy no longer exhibits a tie line corresponding to the heat capacity peak at $P = 0.150$ and $T \approx 1.25$, which confirms that $P = 0.150$ is indeed above the critical point. Therefore, the liquid-gas coexistence curve seems to be consistent (at least within finite-size effects) with the location of the expected critical point. The solid-liquid coexistence temperatures systematically underestimate the tail corrected values,[38,39] which is to be expected, by roughly 5%-10%. Additional contributions to the difference are finite-size effects and the fixed unit cell shape. The cubic cell shape leads to a crystalline solid with defects that does not correspond

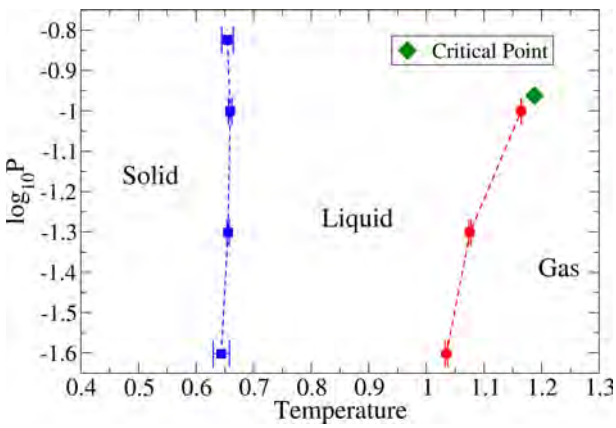

FIG. 10. Portion of the pressure-temperature phase diagram for the cubic unit cell periodic LJ system of 128 particles and pair-wise interaction cutoff $r_c = 2.5$. Note that the error bars are horizontal in the temperature value. The dashed lines were added to help guide the eye. The critical point corresponds to the critical temperature $T_c = 1.1876(3)$ and critical pressure $P_c = 0.1093(6)$ previously reported by Wilding.[35,36]

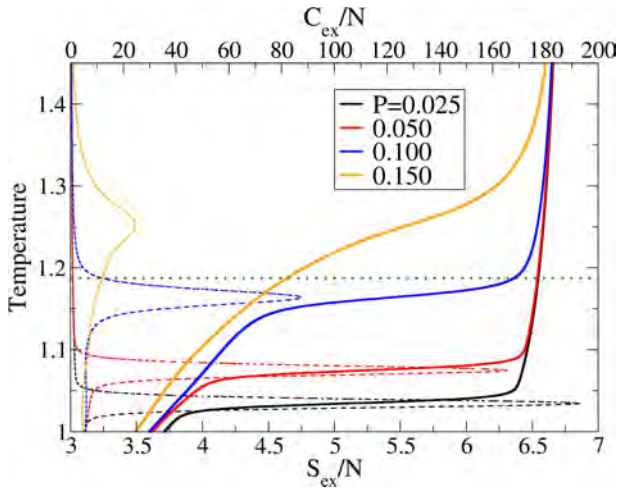

FIG. 11. Temperature versus excess per particle entropy and heat capacity in the vicinity of the liquid-gas coexistence. Solid lines are the entropy across the bottom x axis and dashed lines the heat capacity across the top x axis. These results are from a single simulation at each of the simulated pressures and therefore no error bars are given. The green dotted line is the critical temperature $T_c = 1.187(3)$ reported by Wilding.[35]

to the global minimum crystal structure. This issue can be dealt with by implementing a variable cell shape simulation, the details of which are outlined in Section IV C.

C. Extension to variable cell shape systems

The variable cell shape system is allowed to sample various non-orthogonal cell shapes.[40–42] In these systems the simulation cell is represented by a 3×3 matrix[40] $h = \{a, b, c\}$ in which a, b, and c are the vectors representing the cell edges. The volume is then given by the determinant[42] $V = \det h$.

The actual implementation of IBNS, as given in Section II, is essentially unchanged for these systems. However, the NPT partition function can be rewritten in terms of the cell matrix,[43]

$$\Delta_{ex} = \int_0^{V_{max}} dV\, V^N \int dh_0 \int_0^1 ds\, e^{-\beta H} \times \delta(h_0 - 1), \quad (23)$$

where $h_0 = hV^{-1/3}$, the enthalpy is now $H = PV + E(sh_0V^{1/3})$, and the scaled coordinate is now $s = xh_0^{-1}V^{-1/3}$. Then rewriting in terms of the normalized athermal probability density, $p(V, h_0, s) = V^N/K$, the partition function is

$$\Delta_{ex} = K \int_0^{V_{max}} dV \int dh_0 \int_0^1 ds\, p(V, h_0, s) e^{-\beta H} \times \delta(h_0 - 1), \quad (24)$$

with $K = V_{max}^{N+1}/(N+1)$. If isobaric phase space points were drawn at random from $p(V, h_0, s)$, Eq. (24) could be reduced to a simple average over the enthalpy evaluated at those points (Eq. (11)). Therefore, the sample points are still cataloged simply by their enthalpy when IBNS is performed. The main difference between the variable shape system and the fixed shape system is in the Monte Carlo sampling implementation, in which the volume deformation move is replaced by a more generic cell deformation move. In general, the cell deformation consists of a random perturbation of one or more elements of h and can change both the shape and/or volume of the simulation cell. The fact that the variable cell shape can access different shapes with the same volume can be factored into the implementation of trial moves. Indeed, it has been suggested[44] that the cell deformation move is more effective when split into independent shape-conserving volume changes and volume-conserving shape changes. Regardless of the choice of trial move implementation, cell deformations that result in a volume change are drawn from $p(V, h_0, s)$ using a Markov chain with the same volume acceptance criteria of Eq. (12). Assuming that $f = 1/2$ is used the IBNS algorithm for the variable cell shape system is as follows:

1. Select a constant pressure value, P;
2. sample values of enthalpy according to $p(V, h_0, s)$ while enforcing $V \le V_{max}$;
3. determine the median enthalpy, H_m, of the enthalpy values sampled in the previous step;
4. sample values of enthalpy according to $p(V, h_0, s)$ under the conditions $H < H_m$ and $V \le V_{max}$; and
5. repeat steps 3 and 4 until some convergence/stopping criterion is met.

After the simulation is complete, the median enthalpy values (H_m) are used to approximate the excess partition function using Eq. (13). The extension of IBNS to simulations involving solids is therefore straightforward, at least in principle. However, as previously demonstrated by Pártay *et al.* in NS simulations of clusters,[7] it can be difficult to properly sample multimodal energy landscapes and converge to the global potential minimum. Analogously, in the isobaric case it may be difficult to converge to the defect free crystal. Therefore, the use of advanced/smarter samplers, such as the multiple walker style implemented by Pártay *et al.*,[7] diffusive,[11,29] or superposition enhanced[30] NS, will likely be necessary for studies of phase transitions involving solids.

V. CONCLUSIONS

We have successfully extended the atomic simulation framework of nested sampling to isobaric systems. We wrote the excess NPT partition function as an expectation value with respect to the probability density V^N/K, where V is the volume, N is the number of particles, and K is a normalization constant. This athermal probability density is then iteratively sampled in a nested manner, each time eliminating a high-enthalpy portion corresponding to half of the remaining isobaric phase space volume. After converging to a local minimum in the enthalpy landscape, the nested sampling data are used to compute the partition function and all related thermodynamic quantities at any temperature. Explicit expressions were given for key quantities.

The IBNS method was demonstrated by simulating finite Lennard-Jones systems with $N = 17$ and $N = 55$ atoms at pressures $P = 0.001$, 0.01, 0.1, and 1.0. The heat capacity and density for these systems as functions of temperature were shown to be in good agreement with those from parallel tempering Monte Carlo simulation, validating the method. The simulations captured both the liquid-gas and solid-liquid transitions at low pressure and the pressure effects on these transitions were discussed. It was also demonstrated

that at sufficiently high pressure ($P = 1.0$), the liquid-gas transition disappeared and these finite LJ systems likely attain a supercritical fluid-like state. The increase in the transition temperatures with pressure reported in previous publications was confirmed. Plots of the temperature versus entropy highlighted the decreased entropy change across the phase transitions with pressure, and further analysis of the heat capacity data allowed simple phase diagrams to be constructed. Although demonstrated on finite (non-periodic) systems, this new IBNS method should be easily applied to any isobaric system, including condensed phase systems.

Additional simulations of finite Lennard-Jones systems with $N = 17$ atoms were run in order to demonstrate how various nested sampling parameter choices affect the simulation quality and thermodynamics results. In practice, an upper volume cutoff must be imposed which sets the value of K. It was shown that the choice of the upper volume cutoff has the largest effect on the accuracy of the quantities directly dependent on the logarithm of the partition function, but that the thermodynamic quantities that depend on derivatives of the logarithm of the partition function are much less sensitive to its value. Therefore, the upper volume cutoff can serve as a tunable parameter between the accuracy and efficiency of computing the desired quantities. It was shown that an upper potential energy cutoff can be enforced in conjunction with the required upper volume cutoff. In addition, it was shown that the Markov chain length can have a direct impact on the quality of the nested enthalpy values.

The IBNS method was further demonstrated on a simple periodic system consisting of Lennard-Jones particles in a cubic unit cell. A portion of the pressure-temperature phase diagram was computed. The liquid-gas coexistence was found to be consistent with the critical point reported in previous studies. In addition, the update of the Monte Carlo sampling scheme to simulate variable cell shape systems was outlined.

This new athermal method readily handles phase transitions with no additional optimization and is ideal for studying first-order phase transitions of systems under constant pressure. The isobaric nested sampling method also provides a powerful, yet straightforward alternative to NPT parallel tempering Monte Carlo. A crude relative efficiency comparison suggested that even with the simple sampling routine implemented in this work, isobaric nested sampling was able to achieve a roughly 2.5 times sampling efficiency gain over NPT parallel tempering in computing the heat capacity of the finite LJ systems. The use of more sophisticated and efficient sampling routines could likely dramatically increase this efficiency gain. Further work may be done in applying the IBNS method to more complicated systems and systems with flexible simulation cells.

[1]A. Gelman and X.-L. Meng, Stat. Sci. **13**, 163 (1998).
[2]N. Metropolis, A. W. Rosenbluth, M. N. Rosenbluth, A. H. Teller, and E. Teller, J. Chem. Phys. **21**, 1087 (1953).
[3]*Free Energy Calculations: Theory and Applications in Chemistry and Biology*, Springer Series in Chemical Physics, edited by C. Chipot and A. Pohorille (Springer, Berlin, 2007).
[4]T. A. Pascal, D. Schärf, Y. Jung, and T. D. Kühne, J. Chem. Phys. **137**, 244507 (2012).
[5]H. Meirovitch, Curr. Opin. Struct. Biol. **17**, 181 (2007).
[6]S. Singh, M. Chopra, and J. J. de Pablo, Annu. Rev. Chem. Biomol. Eng. **3**, 369 (2012).
[7]L. B. Pártay, A. P. Bartók, and G. Csányi, J. Phys. Chem. B **114**, 10502 (2010).
[8]J. Skilling, AIP Conf. Proc. **735**, 395 (2004).
[9]J. Skilling, J. Bayesian Anal. **1**, 833 (2006).
[10]N. S. Burkoff, C. Várnai, S. Wells, and D. Wild, Biophys. J. **102**, 878 (2012).
[11]H. Do, J. D. Hirst, and R. J. Wheatley, J. Chem. Phys. **135**, 1 (2011).
[12]H. Do, J. D. Hirst, and R. J. Wheatley, J. Phys. Chem. B **116**, 4535 (2012).
[13]H. Do and R. J. Wheatley, J. Chem. Theory Comput. **9**, 165 (2013).
[14]S. O. Nielsen, J. Chem. Phys. **139**, 124104 (2013).
[15]L. B. Pártay, A. P. Bartók, and G. Csányi, Phys. Rev. E **89**, 022302 (2014).
[16]M. E. Tuckerman, *Statistical Mechanics: Theory and Molecular Simulation*, Oxford Graduate Texts (Oxford University Press, USA, 2010).
[17]D. Frenkel and B. Smit, *Understanding Molecular Simulation, Second Edition: From Algorithms to Applications*, Computational Science, 2nd ed. (Academic Press, 2001).
[18]E. Marinari and G. Parisi, EPL **19**, 451 (1992).
[19]M. Saito and M. Matsumoto, in *Monte Carlo and Quasi-Monte Carlo Methods 2008*, edited by P. L' Ecuyer and A. B. Owen (Springer, Berlin Heidelberg, 2009), pp. 589–602.
[20]D. Sabo, D. L. Freeman, and J. D. Doll, J. Chem. Phys. **122**, 094716 (2005).
[21]F. Calvo and J. P. K. Doye, Phys. Rev. B **69**, 125414 (2004).
[22]W. D. Kristensen, E. J. Jensen, and R. M. J. Cotterill, J. Chem. Phys. **60**, 4161 (1974).
[23]H.-P. Cheng, X. Li, R. L. Whetten, and R. S. Berry, Phys. Rev. A **46**, 791 (1992).
[24]W. Ortiz, A. Perlloni, and G. E. López, Chem. Phys. Lett. **298**, 66 (1998).
[25]F. H. Verhoek, J. Chem. Educ. **47**, 286 (1970).
[26]V. A. Mandelshtam and P. A. Frantsuzov, J. Chem. Phys. **124**, 204511 (2006).
[27]J. P. K. Doye, M. A. Miller, and D. J. Wales, J. Chem. Phys. **111**, 8417 (1999).
[28]A. Barducci, G. Bussi, and M. Parrinello, Phys. Rev. Lett. **100**, 020603 (2008).
[29]B. J. Brewer, L. B. Pártay, and G. Csányi, Stat. Comput. **21**, 649 (2011).
[30]S. Martiniani, J. D. Stevenson, D. J. Wales, and D. Frenkel, Phys. Rev. X **4**, 031034 (2014).
[31]N. Chopin and C. P. Robert, Biometrika **97**, 741 (2010).
[32]D. A. Kofke, J. Chem. Phys. **121**, 1167 (2004).
[33]H. G. Katzgraber, S. Trebst, D. A. Huse, and M. Troyer, J. Stat. Mech.: Theory Exp. **2006**, P03018 (2006).
[34]R. W. Henderson and P. M. Goggans, AIP Conf. Proc. **1636**, 100 (2014).
[35]N. Wilding, Phys. Rev. E **52**, 602 (1995).
[36]N. Wilding and K. Binder, Phys. A **231**, 439 (1996).
[37]J. J. Potoff and A. Z. Pangiotopoulos, J. Chem. Phys. **109**, 10914 (1998).
[38]G. C. McNeil-Watson and N. B. Wilding, J. Chem. Phys. **124**, 064504 (2006).
[39]E. A. Mastny and J. J. de Pablo, J. Chem. Phys. **127**, 104504 (2007).
[40]M. Parrinello and A. Rahman, J. Appl. Phys. **52**, 7182 (1981).
[41]R. Najafabadi and S. Yip, Scr. Metall. **17**, 1199 (1983).
[42]S. Yashonath and C. N. R. Rao, Mol. Phys. **54**, 245 (1985).
[43]G. J. Martyna, D. J. Tobias, and M. L. Klein, J. Chem. Phys. **101**, 4177 (1994).
[44]J. de Graaf, L. Filion, M. Marechal, R. van Roij, and M. Dijkstra, J. Chem. Phys. **137**, 214101 (2012).

Nested Sampling of Isobaric Phase Space for the Direct Evaluation of the Isothermal-Isobaric Partition Function of Atomic Systems

Citation:

Wilson, Blake A., Lev D. Gelb, and Steven O. Nielsen. 2015. "Nested sampling of isobaric phase space for the direct evaluation of the isothermal-isobaric partition function of atomic systems." The Journal of Chemical Physics 143(15), doi:10.1063/1.4933309.